HailTrack—Improving Radar-Based Hailfall Estimates by Modeling Hail Trajectories

JORDAN P. BROOK,[a] ALAIN PROTAT,[b] JOSHUA SODERHOLM,[b] JACOB T. CARLIN,[c,d] HAMISH MCGOWAN,[a] AND ROBERT A. WARREN[e]

[a] *Atmospheric Observations Research Group, University of Queensland, Brisbane, Queensland, Australia*
[b] *Radar Science and Nowcasting, Science and Innovation Group, Australian Bureau of Meteorology, Docklands, Victoria, Australia*
[c] *Cooperative Institute for Mesoscale Meteorological Studies, University of Oklahoma, Norman, Oklahoma*
[d] *NOAA/OAR/National Severe Storms Laboratory, Norman, Oklahoma*
[e] *School of Earth, Atmosphere and Environment, and Centre of Excellence for Climate Extremes, Monash University, Melbourne, Victoria, Australia*

ABSTRACT: A spatial mismatch between radar-based hail swaths and surface hail reports is commonly noted in meteorological literature. The discrepancy is partly due to hailstone advection and melting between detection aloft and observation at the ground. This study aims to mitigate this problem by introducing a model named HailTrack, which estimates hailfall at the surface using radar observations. The model operates by detecting, tracking, and collating hailstone trajectories using dual-polarized, dual-Doppler radar retrievals. Notable improvements in hailfall forecasts were observed through the use of HailTrack, and initializing the model with radar retrievals of hail differential reflectivity H_{DR} was found to produce the most accurate hailfall estimates. The analysis of a case study in Brisbane, Australia, demonstrated that trajectory modeling significantly improved the correlation between hail swaths and hail-related insurance losses, increasing Heidke skill scores from 0.48 to 0.58. The accumulated kinetic energy of hailstone impacts also showed some skill in identifying areas that were exposed to particularly severe hailfall. Other unique impact estimates are presented, such as hailstone advection information and hailstone impact angle statistics. The potential to run the model in real time and produce short-term (10–15 min) nowcasts is also introduced. Model applications include improving radar-based hail climatologies, validating hail detection techniques and insurance claims data, and providing real-time hail impact maps to improve public awareness of hail risk.

KEYWORDS: Hail; Radars/Radar observations; Remote sensing; Nowcasting; Numerical analysis/modeling

1. Introduction

Hailstorms pose a significant risk to life and property in many parts of the world, resulting in over USD 1 billion in insured losses annually (Jewell and Brimelow 2009; Sander et al. 2013). The economic cost of hail damage highlights the need to develop capabilities to accurately quantify the spatial extent and intensity of hail impacts on the ground. The areal extent of hail swaths, in combination with hail intensity metrics such as maximum hail diameter or hail kinetic energy, form the basis of hail climatologies and hail damage modeling in the insurance industry (e.g., Kunz and Puskeiler 2010). Accurate hail swath information is also important for assessing the ability to detect hail by radar, understanding hailstorm dynamics and microphysics, and verifying high-resolution numerical weather model predictions (Changnon 1970; Snook et al. 2016).

A review of hail literature reveals four common approaches for estimating the extent of hail impacts, namely, using hail reports (e.g., Zhang et al. 2008; Ortega et al. 2009; Allen et al. 2015; Kahraman et al. 2016; Allen and Allen 2016; Jin et al. 2017), in situ measurements such as hail pads (e.g., Changnon 1968; Auer and Marwitz 1972; Smith and Waldvogel 1989; Fraile et al. 1999), insurance claims data (e.g., Hohl et al. 2002; Schuster et al. 2006; Brown et al. 2015; Warren et al. 2019), and

weather radar imagery (e.g., Basara et al. 2007; Cintineo et al. 2012; Ortega 2018). Issues such as population bias, reporting insufficiency and secular trends from population changes and reporting practices plague all of these data sources except those derived from weather radar (Allen et al. 2015; Ortega 2018). Estimates made from radars also benefit from fine spatiotemporal resolution, measurement homogeneity and the ability to measure in three dimensions. These benefits make radar-based hail impact estimates a compelling option for quantifying the footprint of hail events.

Despite the observational advantages of using radars to predict hail impacts, it remains a challenging task. First, hail detection and sizing by radar is essentially an underresolved problem as size, liquid water content and distribution, and the number concentration of hailstones all contribute to a volume's backscattering characteristics. This leads to a high level of uncertainty when using radars to estimate hail size distributions aloft (Depue et al. 2007; Wilson et al. 2009; Blair et al. 2011; Ortega 2018). Further uncertainty is introduced when radar-based hail retrievals are used to estimate the extent and intensity of hailfall on the ground (Schiesser 1990; Hohl et al. 2002; Schuster et al. 2006). Most attempts at comparing radar measurements directly to hail observations at ground level introduce two implicit assumptions: 1) hailstone sizes remain constant from detection aloft until impact, and 2) hailstones land directly below where they are detected aloft. This study aims to relax these assumptions by modeling hailstones from

detection aloft to their expected impact locations. We expect this approach to significantly improve the skill of hailfall estimates, while acknowledging that the inherent uncertainty in estimating hail sizes with radar data places an upper bound on the potential accuracy of such endeavors.

Previous hail trajectory and impact mapping studies have shown that hailstones can advect considerable distances from their initial position aloft to their impact position on the ground, affecting the ability to match radar-based hail observations directly to ground truth (Schiesser 1990; Schmid et al. 1992; Conway and Zrnić 1993; Hohl et al. 2002; Schuster et al. 2006; Warren et al. 2019). Many studies use low-level tilts of volumetric radar scans to mitigate the effects of advection as hailstones at lower altitudes have less potential to advect large distances (e.g., Depue et al. 2007; Ortega et al. 2016). However, this approach is not suited for nowcasting purposes as it reduces the lead time for hail warnings and effectively extends the interval between subsequent radar measurements by omitting higher elevation tilts. Furthermore, the use of exclusively low-level scans is not feasible for vertically integrated hail retrievals such as maximum expected size of hail (MESH) and vertically integrated liquid (VIL) (Greene and Clark 1972; Witt et al. 1998). To mitigate the effects of advection, many radar validation studies use a neighborhood approach when matching radar-derived swaths to ground truth. This can involve matching hail reports to radar-derived properties anywhere within the spatiotemporal bounds of a storm (Blair et al. 2011; Ortega 2018), within a predefined radius around each hail report (Nanni et al. 2000; Cintineo et al. 2012; Warren et al. 2019) or more complex methods based on the vertical reflectivity distribution (Ortega et al. 2016). The use of these matching techniques reflects the inability of current radar-based hail retrievals to adequately predict the spatial extent and location of hail swaths on the ground.

Previous research has also attempted to improve the point-to-point match between radar products and ground truth by shifting radar-based swaths horizontally to account for hailstone advection. This has been demonstrated to significantly improve the correlation of radar-derived swaths with crop damage (Schiesser 1990), hailpad impacts (Schmid et al. 1992), and insurance claims (Hohl et al. 2002; Schuster et al. 2006). While this type of advection correction does improve damage estimates, its accuracy and applicability are limited. First, assuming a constant advection displacement for the entire radar swath does not consider that hailstones with different terminal velocities and different initial altitudes will advect different distances. Second, these corrections rely on high-resolution ground-truth observations to derive a representative swath displacement vector. This technique is therefore not suitable for use in regions with limited hail observations or in real-time nowcasting applications. A study by Schiesser (1990) is an exception to the simple, uniform horizontal shift method. The authors account for the height of hail observations and advect hailstones with a constant horizontal velocity. A representative horizontal velocity vector for the whole storm is selected by optimizing the correlation between radar measurements and hail-pad impacts. Once again, this method underresolves the complexity of hail advection calculations by

assuming constant velocities for all hailstones and constant wind speeds throughout each storm.

The model presented here (subsequently referred to as HailTrack) targets the aforementioned limitations involved with associating radar retrievals aloft to hail observations on the ground. We introduce a trajectory modeling approach that uses radar data to predict the areal extent and intensity of hailfall at the surface. The aim of this new approach is to improve current radar-based hail impact predictions by directly modeling the effects of hailstone advection and melting. The HailTrack method is first outlined in section 2, and it is subsequently validated using insurance data from an Australian case study in section 3. A more in-depth hail trajectory analysis is included in section 4, followed by a brief discussion on model sensitivity in section 5. A summary of the findings from this study and a discussion of future research directions are provided in section 6.

2. HailTrack method

a. Overview

The method introduced in this study requires a representative thermodynamic profile of the atmosphere (e.g., radiosonde or numerical model data) and polarimetric, dual-Doppler radar coverage. Polarimetric information is used to estimate the initial size and position of hailstones within each modeled hailstorm, and dual-Doppler measurements are used to retrieve the three-dimensional wind field. Dual-Doppler observations are required to fully resolve storm-induced wind perturbations and their effects on hail trajectories; however, this requirement limits the method's operational applicability in many radar networks due to the rarity of dual-Doppler coverage. After hailstones are initiated within the model, their trajectories are estimated by modeling their interaction with 3D wind retrievals. Hailstone melting estimates are coupled to the trajectory model to account for reductions in hailstone size and terminal velocity as they fall below the environmental melting level. All hailstones that reach the ground in the model are collated into a unique, advection-corrected hailfall estimate. The remainder of this section describes the implementation of these processes by outlining how methods from the existing literature have been adapted for this purpose. Refer to Fig. 1 for a visual representation of this process.

b. Hail detection and sizing

The trajectory modeling approach used in this study requires a radar-based hail detection and sizing method to initiate hailstone simulations. The requirement for each hail sizing/detection algorithm is to provide a domainwide, numerically continuous hail size and position in three dimensions.

1) HAIL DIFFERENTIAL REFLECTIVITY (H_{DR})

Following a review of hail detection literature, the only continuous, three-dimensional hail size retrieval is based on the hail differential reflectivity, or H_{DR}, parameter. This technique exploits bulk geometric differences between hail and rain distributions by identifying hail as a combination of
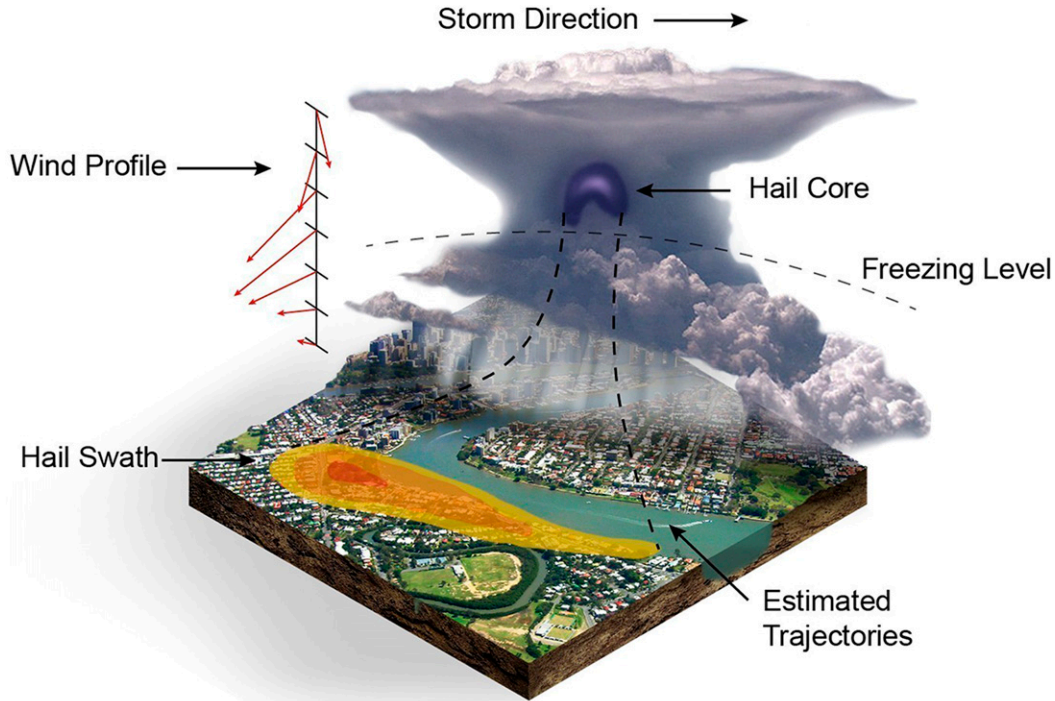
FIG. 1. A schematic showing the physical process of hail advection that motivates this trajectory modeling approach. The image represents an idealized version of hail core advection due to a ground-relative wind profile, resulting in a spatially offset hail swath.

high equivalent horizontal reflectivity Z_H and low differential reflectivity Z_{DR}. The reader is referred to Aydin et al. (1986) for a detailed description of the H_{DR} parameter. Depue et al. (2007) presented an empirical relationship between the H_{DR} parameter and hail size at S band using a collection of 86 hail reports. The approximate H_{DR}–hail size relationship inferred from Depue et al. (2007, their Fig. 5) is as follows:

$$d_{hdr} = \begin{cases} 0; & H_{DR} < 21\,\text{dB} \\ 0.03H_{DR}^2 - 0.37H_{DR} + 11.69; & H_{DR} \geq 21\,\text{dB} \end{cases}, \quad (1)$$

where d_{hdr} is the resulting H_{DR}-based equivolume hail diameter estimate in millimeters; H_{DR} values below 21 dB are assigned a hail diameter of 0 because the H_{DR}–d_{hdr} relationship in Eq. (1) was developed using values above this threshold. The H_{DR} lower bound corresponds to a minimum d_{hdr} hail size estimate of 17 mm (to the nearest millimeter). This "minimum observable size threshold" is applied to all hail retrievals in this study to ensure consistency between approaches. Note that hailstones smaller than this minimum threshold may be large enough to cause crop damage but are unlikely to damage common building materials (Schiesser 1990; Marshall et al. 2002). Depue et al. (2007) noted a large standard deviation of 10.6 mm between hail reports and the hail size relationship introduced above. This highlights the uncertainty involved in estimating one-to-one hail sizes using the H_{DR} parameter. The small ground-truth sample size used to calibrate the H_{DR}–d_{hdr} relationship also limits our confidence in the method. Despite

these concerns, H_{DR} hail sizes have been noted to show skill in detecting the presence of severe hail and are unique in producing three-dimensional, continuous hail size estimates (Aydin et al. 1986; Nanni et al. 2000; Depue et al. 2007; Murillo and Homeyer 2019).

2) MESH

MESH is a single-polarized hail detection algorithm involving a weighted integration of Z_H above the melting level to produce a two-dimensional grid of the maximum estimated hail size at the surface (1 km grid spacing in this study). Refer to Witt et al. (1998) for a full description of the MESH method. Two-dimensional MESH grids are not immediately applicable to this study as three-dimensional hail retrievals are required to initiate trajectories. To resolve this problem, the MESH estimates are extended into three dimensions by linearly varying MESH values according to the corresponding vertical Z_H profile (in decibel units, with 0.5-km vertical grid spacing). Cartesian gridding of radar variables is performed with the Barnes (1964) weighting scheme and a constant, 2-km radius of influence using the Python ARM Radar Toolkit (Py-ART; Helmus and Collis 2016). The resulting three-dimensional MESH hail size estimate d_{mesh} is formalized below:

$$d_{mesh} = \frac{Z_H}{Z_{H,max}} \text{MESH}, \quad (2)$$

where $Z_{H,max}$ is the maximum reflectivity in the column. This formulation ensures that for each column d_{mesh} is equal to the

two-dimensional MESH value at the altitude with the highest reflectivity while the d_{mesh} values below and above decrease proportional to the vertical Z_H profile.

The accuracy of the 3D MESH formulation above [defined as d_{mesh} in Eq. (2)] is limited by two main factors: 1) Z_H does not vary proportionately to hail size as it is also influenced by hydrometeor geometry, liquid water coating, and number concentration; and 2) the underlying MESH estimates used in Eq. (2) have been shown to exhibit limited skill in estimating one-to-one hail sizes when compared with hail reports (Witt et al. 1998; Wilson et al. 2009; Ortega 2018). In light of these limitations, d_{mesh} should be interpreted solely as a means of initiating hail trajectories within HailTrack and is not intended as a stand-alone hail retrieval method. The investigation of this retrieval method within HailTrack represents an attempt to account for the effects of storm-driven hail advection in conventional MESH estimates. These efforts are motivated by the persistent use of MESH for hail detection in operational forecasts and historical datasets, especially in regions such as Australia with predominantly single-polarized radar coverage (Richter and Deslendes 2007; Warren et al. 2019).

3) H_{DR}-WEIGHTED HSDA HYBRID APPROACH

Fuzzy-logic algorithms have superseded the more empirical approaches previously used for hydrometeor classification algorithms (HCA). These techniques are better suited to hail detection as they provide a framework to handle the uncertainty involved in classifying hydrometeor types from radar data (Park et al. 2009). Hail is separated from other hydrometeor types in this study using S-band modifications to the HCA outlined in Dolan and Rutledge (2009) and Dolan et al. (2013). The hail size discrimination algorithm (HSDA) is applied following the HCA classifications by dividing the "hail" category into "small" (<25 mm), "large" (25–50 mm), and "giant" (>50 mm) hail size classes. These size classifications are used throughout the text to ensure consistency in hail size nomenclature. For a detailed description of the HSDA method, refer to Ryzhkov et al. (2013a,b). HSDA hail size retrievals cannot be implemented directly in HailTrack due to their categorical hail size outputs. Instead, H_{DR} retrievals are used to introduce a continuous hail size spectrum within each HSDA class. Hail sizes are varied proportionally to the H_{DR} values within each size class. Therefore, small hail varies between 0 and 25 mm and large hail varies between 25 and 50 mm. The giant category introduces additional complexity because of the absence of a prescribed upper bound.

Accurately estimating the maximum hail size within an entire storm using radar data is a difficult task. MESH is commonly used operationally for this purpose despite the aforementioned limitations in estimating one-to-one sizes. In the absence of a more robust, radar-based maximum hail size estimation technique, we use a stationary 75-mm (~3 in.) upper bound for all giant HSDA classifications. For giant hailstones, the absolute size has a limited effect on the uncertainty of trajectory calculations, as large terminal velocities associated with giant hailstones limit the potential for advection in the presence of horizontal winds. To confirm this, we consider the sensitivity of the model to the arbitrarily

chosen hail size upper bound by varying this predefined "maximum" hail size in section 3. The hail size classifications for this method are summarized as follows:

$$
d_{hsda} = \begin{cases} 25\dfrac{d_{hdr} - d_{S,min}}{d_{S,max} - d_{S,min}}; & \text{HSDA} = \text{small} \\[2ex] 25\dfrac{d_{hdr} - d_{L,min}}{d_{L,max} - d_{L,min}} + 25; & \text{HSDA} = \text{large} , \\[2ex] 25\dfrac{d_{hdr} - d_{G,min}}{d_{G,max} - d_{G,min}} + 50; & \text{HSDA} = \text{giant} \end{cases} \quad (3)
$$

where $d_{S,min}$ is the minimum d_{hdr} value within the small HSDA size class, $d_{G,max}$ is the maximum d_{hdr} value within the giant HSDA class, and so on. This approach should allow further size discrimination within each HSDA class because d_{hdr} theoretically varies proportionally with hail size.

c. 3D wind retrievals

Accurate trajectory modeling requires a realistic estimate of the three wind components within the hailstorm. This study follows the method outlined in Protat and Zawadzki (1999) by using dual-Doppler data to resolve the three-dimensional wind field. The reader is referred to Protat and Zawadzki (1999) and Collis et al. (2013) for a complete description of this method. 3D wind calculations are performed in a Cartesian coordinate system with a horizontal resolution of 1 km and a vertical resolution of 500 m. The ground-based radars used in this study are not suited to sampling near-surface altitudes due to the effects of ground clutter and beam divergence at increasing range. As a result, the lowest altitude for the 3D wind retrieval is 500 m above sea level. Reflectivity–fall speed relationships reported in Conway and Zrnić (1993) are applied based on HCA classifications to account for errors in vertical velocities due to the suspension of large hydrometeors. Regions with nearly collinear beam orientations between radars are discounted from the analysis due to the requirement for dual-Doppler measurements. We define these nearly collinear regions where the cosine of the angle between the two radar beams is greater than 0.95. The resulting dual-Doppler lobes (e.g., Fig. 3) ultimately limit the wind retrieval domain and the maximum effective range of the HailTrack method.

The gaps resulting from these nearly collinear regions, along with weak echo regions, present an issue for hail trajectory modeling as a small portion of hail simulations may fall into such regions with missing 3D winds data. When this occurs in the model, a gap-filling method is used to find a representative velocity value. In missing wind data regions, the vertical wind velocity is set to zero and the horizontal components are set to the mean value of the horizontal velocity in the closest horizontal cross section. This method allows hailstones that fall out of precipitating regions or out of the Doppler lobes to continue advecting with the altitude-specific mean velocity value until they reach the ground or reenter an area of valid velocity values. The inclusion of the gap filling method greatly improves the spatial continuity of hail swaths, especially for storms that move through the nearly collinear region between the radars.

d. Microphysical considerations

Melting plays an important role in altering the terminal velocities of hailstones as they fall (Rasmussen et al. 1984). A melting process is implemented within HailTrack using the model presented by Ryzhkov et al. (2013a, hereinafter R13A). Hailstone mass losses occur due to thermodynamic processes such as sublimation and evaporation, as well as the meltwater shedding parameterization introduced by R13A. Thermodynamic environmental variables used in the model are sourced from a representative vertical profile (e.g., radiosonde or numerical model data) for each individual storm. No hail growth processes are simulated due to the inability to accurately estimate environmental variables such as supercooled liquid water content in real time using current remote sensing methods. The initial density of hailstones aloft follows modeling experiments by Rasmussen and Heymsfield (1987), which assume hailstone densities increase with size from small, low density graupel (600 kg m^{-3}) to large stones composed of roughly solid ice (917 kg m^{-3}). This size-dependent density function was also employed in R13A (their Fig. 1), and is written as follows:

$$\rho_0(d) = \begin{cases} 600 - 0.25d^2 + 17.61d; & d < 36\,\text{mm} \\ 917; & d \geq 36\,\text{mm} \end{cases}, \quad (4)$$

where ρ_0 is the prescribed initial hailstone density. The true density ρ of a hailstone at any subsequent point along its trajectory is calculated with consideration to the accumulation of meltwater within internal air cavities and on the hailstone exterior. For a comprehensive thermodynamic description on the melting model used and its effects on hailstone terminal velocities, the reader is referred to the appendix material in R13A.

e. Trajectory modeling and collation

It is currently not possible to accurately estimate hail size distributions aloft using polarimetric weather radar information. Therefore, instead of attempting to simulate a representative size distribution, trajectories are initiated based on the maximum expected hail size within each grid box (MESH) or radar voxel (H_{DR}, HSDA). This approach captures the spatial distribution of the most damaging hail while avoiding any assumptions about hail distributions in the atmosphere. Initial maximum size estimates are based on the hail detection/sizing methods discussed earlier. The only forcing mechanisms for hailstone trajectories are gravity and drag from the 3D wind field. At every point along their trajectory, horizontal components of the wind field (u, v) are used as the horizontal hydrometeor velocity, and vertical velocities are the sum of vertical air velocity w and the terminal velocity V_T. Therefore, the true velocity vector for hydrometeors as they move through the atmosphere is (u, v, $V_T + w$). Using this velocity vector, positions at a new time step n can be calculated on the basis of the previous step ($n - 1$):

$$x_n = x_{n-1} + u_{n-1}\Delta t$$
$$y_n = y_{n-1} + v_{n-1}\Delta t$$
$$z_n = z_{n-1} + (V_T + w_{n-1})\Delta t, \quad (5)$$

where Δt is the time step. A time step of 10 s was deemed sufficient for avoiding truncation errors after considering the maximum expected updraft velocities and the vertical grid spacing of wind retrievals (Ziegler et al. 1983; Conway and Zrnić 1993). Terminal velocities are updated at each time step and new positions are calculated until the hailstone trajectory intersects the ground. 3D wind fields are not temporally adjusted or spatially shifted according to storm motion between radar scans as the temporal resolution of operational radar scans (~6-min volumes) is deemed sufficient to capture the evolution of the wind field for hailstones with significant durations aloft. In this implementation, the nearest-neighbor method was chosen to interpolate 3D winds to exact hailstone positions in an effort to achieve the computational efficiency required for real-time operations. More accurate interpolation methods (e.g., trilinear) could be used in applications where computational efficiency is not prioritized. Once hailstones hit the ground, variables such as initial diameter, final diameter, initial position, final position, impact velocity, and trajectory duration are stored. Two analyses are then derived from all simulated hailstone impacts on 1-km^2 grids at the surface: 1) a maximum hail size swath and 2) a cumulative kinetic energy field KE$_H$. KE$_H$ calculations are formalized below:

$$\text{KE}_H = \sum_{i=0}^{n} \frac{1}{2} m_i V_i^2 = \sum_{i=0}^{n} \frac{1}{12} \pi \rho_i d_i^3 \left[u_i^2 + v_i^2 + (V_{T,i} + w_i)^2 \right], \quad (6)$$

where m is hailstone mass, ρ is hailstone density, d is hailstone equivolume diameter, n is the number of hailstone impacts within each grid square, and the subscript i indicates a hailstone-specific property for the ith hailstone impact within each grid square. Equation (6) underestimates the total kinetic energy of hail impacts because only a single, maximum size hailstone is initialized per voxel/grid point, per radar scan. Accordingly, we normalize KE$_H$ values between 0 and 1 to indicate that this statistic should be interpreted as a "storm specific" measure and should only be used to highlight regions with the most intense hailfall within an event. A 3×3 median filter is employed to reduce speckle noise and increase readability in maximum size and KE$_H$ swaths (Lakshmanan et al. 2013).

f. Model validation

Conventional radar-based hail impact swaths based on hail detections aloft (MESH, H_{DR}, and vertical maximum reflectivity) are calculated in this study to compare with trajectory-based HailTrack swaths. Conventional swaths are calculated by accumulating the maximum values for each parameter on a 1-km grid throughout the storm lifetime. However, the temporal resolution of radar volumes (~6 min) introduces spatial discontinuities between consecutive radar scans due to storm motion. A cell-tracking technique is used to identify and match cells between radar scans in order to interpolate discontinuous swaths spatially along the storm path. For more information on the cell identification and matching techniques used in this study, the reader is referred to Lakshmanan et al. (2009) and

Dixon and Wiener (1993), respectively. Intermediate grid points between radar scan times are interpolated by shifting the cell at time t forwards, and the cell at time $t + 1$ backward along the storm motion vector. The resulting value of the intermediate grid points is then a linear combination of the values at time t and $t + 1$, weighted by their temporal proximities. The result is a spatially contiguous hail swath capable of providing a robust comparison to the trajectory-based swaths calculated in this study.

Insurance data are used as a validation dataset for the occurrence of damaging hail due to a lack of hail reports. Hail-related insurance claims were provided by Suncorp Insurance and are collated into daily 1-km grids comprising the number of insurance claims and the number of contracts. Refer to Warren et al. (2019) for more details on the Suncorp Insurance dataset. The extent of damaging hail is estimated by creating a binary damage grid (1 for hail damage, 0 for no damage, and −1 for no data), and a damage intensity metric is defined as the percentage of insurance contracts that made hail-related damage claims during the event. Various hail size thresholds are tested for each hail size estimation method to determine the strongest correlation with damaging hail at the corresponding grid points. If the swath value at a point exceeds the threshold, a positive prediction is made and if the value is less than the threshold, a negative prediction is made. By comparing these predictions to the actual binary insurance grid, contingency tables are developed containing true positives a, false positives b, false negatives c, and true negatives d. Contingency tables are used to derive common verification statistics such as the probability of detection (POD), false-alarm rate (FAR), and critical success index (CSI; Schaefer 1990). To compare validation values with recent literature, Heidke skill scores (HSS; Heidke 1926) are also calculated as follows:

$$HSS = 2(ad − bc)/[(a + c)(c + d) + (a + b)(b + d)]. \quad (7)$$

The number of correct forecasts is scaled by the number expected due to chance in the HSS formulation, ensuring scores measure only the fractional improvement of the forecast method (Doswell et al. 1990). Optimum hail size thresholds for each hail detection method are defined as the threshold that produces the highest HSS as it is considered the most robust validation statistic.

3. Model validation

In this section we validate the HailTrack method using a case study from 27 November 2014, in Brisbane, Australia. The hailstorm followed a northerly path through the densely populated Brisbane metropolitan area between 0500 and 0800 UTC, generating an estimated AUD 1.54 billion in insurance losses and roughly 7000 hail-related claims in the Suncorp Insurance dataset (Insurance Council of Australia 2017). These significant financial impacts reflect the contribution of giant hailstones (~70 mm), strong surface level winds (39 m s^{-1} gusts), and the event timing (weekday during the evening rush hour; Parackal et al. 2015). Dual-Doppler data are sourced from two S-band radars, the Mount Stapylton operational weather radar and the CP-2 dual-polarization

research radar (1.0° and 0.93° half-power beamwidths, respectively; Protat and Soderholm 2020). All hail retrievals are performed using the CP-2 radar due to its polarimetric capabilities. Atmospheric inputs to the melting model are sourced from a 0400 UTC sounding at Brisbane Airport (YBBN; ~10 km northeast of Brisbane central business district). While the sounding data may not fully resolve the complexities of the near-storm thermodynamic profile, or its evolution in the 1–2 h preceding the event, we deem its spatiotemporal proximity appropriate for use in the hailstone melting model. The sensitivity of the model to changes in these thermodynamic inputs is discussed in section 5.

The ultimate aim of this section is to validate whether HailTrack hailfall predictions outperform other conventional radar-based approaches. In addition, we seek to determine which of the three hail retrieval methods introduced in section 2b (H_{DR}, MESH and HSDA) is the most performant. Hailfall estimates are predominantly verified using insurance loss data in this study due to the small number of hail size reports collected during event. Although they are an extremely valuable source of validation, insurance damage claims can also be influenced by factors beyond the maximum size or intensity of hailfall. These include but are not limited to 1) the spatial density and value of insured assets, 2) the extent of shielding (e.g., from other buildings and trees), 3) the type and age of building components, 4) the extent and size of the damage, 5) other damage types associated with intense rainfall or severe wind gusts, 6) wind speed and direction, and 7) whether contract holders reliably file claims for every instance of damage. Despite these limitations, insurance data have been noted to provide a valuable insight into the extent of damaging hail at the surface, which makes it a suitable choice for validating the results in this study (Hohl et al. 2002; Brown et al. 2015; Warren et al. 2019).

Table 1 contains skill scores calculated by comparing each hail retrieval method to a binary representation of insurance damage as discussed in section 2f. Three retrievals without trajectory corrections are included in this table and are herein referred to as "conventional" swaths. Of the three conventional swaths, a vertical-maximum reflectivity threshold of 64 dBZ is the most skillful predictor of binary insurance damage with a HSS of 0.50. Uncorrected MESH and H_{DR} swaths showed slightly lower HSS values of 0.46 and 0.48, respectively. There is a consensus among previous studies that the optimal MESH threshold for predicting severe hail occurrence (≥25 mm) in a similar spatiotemporal proximity to a storm is around 30 mm (Wilson et al. 2009; Cintineo et al. 2012; Ortega 2018; Murillo and Homeyer 2019; Warren et al. 2019). In this study a MESH threshold of 46 mm showed the most skill for identifying regions with hail-related insurance damage. The significant difference in optimal thresholds from previous studies highlights the alternate method used here. Instead of matching hail reports to either a single, spatiotemporally representative value for an entire storm or within a predefined neighborhood radius, we point match radar-based swaths to a spatial grid. Warren et al. (2019) highlighted the effects of these matching methods by showing that the optimum MESH threshold changed from 44 to 32 mm when increasing the

TABLE 1. Skill scores for each hail detection method used in this study. The optimum threshold is defined as the threshold that produces the highest HSS.

Hail retrieval	Threshold	POD	FAR	CSI	HSS	Description
Reflectivity	64 dBZ	0.53	0.39	0.40	0.50	Reflectivity swath interpolated by tracking cell movement
MESH	46 mm	0.46	0.38	0.36	0.46	MESH swath interpolated by tracking cell movement
H_{DR}	37 mm	0.47	0.36	0.37	0.48	H_{DR} swath interpolated by tracking cell movement
HailTrack HSDA	69 mm	0.48	0.37	0.38	0.48	H_{DR}-weighted HSDA swath corrected using trajectory modeling
HailTrack MESH	24 mm	0.51	0.38	0.39	0.50	MESH swath corrected using trajectory modeling
HailTrack H_{DR}	37 mm	0.60	0.32	0.47	0.58	H_{DR} swath corrected using trajectory modeling

neighborhood radius used to construct contingency tables from 0 km (i.e., gridscale comparisons) to 5 km. Both the difference in matching techniques and the type of ground-truth mean that skill scores for the conventional swaths in Table 1 cannot be reliably compared to previous literature; instead, they have been included to demonstrate the benefit of applying the trajectory model in this study.

HailTrack HSDA hail size retrievals produced the only trajectory modeled swath that did not outperform the conventional swaths. A large 69-mm optimum hail size threshold led to a reasonable probability of detection (0.48), but this is outweighed by a similarly high false alarm ratio (0.37), resulting in a relatively poor Heidke skill score of 0.48. As discussed previously, this hail retrieval method requires a prescribed maximum hail size for giant HSDA classifications, and it is possible that this assumption plays a significant role in the skill scores observed. The sensitivity of the HSDA retrieval method to the prescribed 75 mm maximum size threshold was explored by varying threshold values between 55 and 85 mm. These sensitivity experiments showed only small fluctuations in the skill scores (<0.01), indicating that the accuracy of the HSDA retrieval method is not strongly influenced by the maximum hail size assumption. Instead, we find that the poor skill of the HSDA method is a result of overestimating the number of giant classifications, especially in the earlier stages of storm development. This results in a significant amount of giant hail in areas with no observed insurance damage, leading to a high FAR and poor skill scores.

Conventional MESH and H_{DR} hail swaths improved considerably when HailTrack advection corrections were applied, with HSS values increasing from 0.46 to 0.50 and from 0.48 to 0.58, respectively. The optimum MESH threshold changed from 46 to 24 mm before and after the HailTrack corrections were applied, due to the reflectivity scaling used to extend MESH into three dimensions. The corrected MESH skill score is consistent with Warren et al. (2019) who found HSS values between 0.49 and 0.51 by using a neighborhood radius of 5–7 km to account for hailstone advection. The corrected MESH swath also outperformed the conventional H_{DR} swath, indicating that trajectory corrections to single polarized hail swaths can outperform conventional polarimetric hail swaths. Results for the HailTrack H_{DR} method showed that combining dual-polarized hail retrievals and trajectory corrections produces the most accurate hailfall estimates. Skill scores for the

HailTrack H_{DR} swath with a 37-mm threshold considerably outperformed all other methods tested here. As a result, the H_{DR} approach is recommended as the default hail retrieval method for HailTrack, all subsequent trajectory modeling and verification in this study is performed using this method.

The threshold that optimizes the correlation between HailTrack size swaths and insurance damages may vary when the validation dataset is extended to include a larger set of events. To verify that HailTrack improvements are robust to these changes in the optimum threshold, it is also necessary to verify that HailTrack swaths outperform conventional swaths across a range of hail size thresholds. To this end, the validation metrics in Table 1 were also calculated using hail size thresholds between 0 and 50 mm. The CSI scores for this range of thresholds are shown for both the HailTrack H_{DR} and conventional H_{DR} swaths in Fig. 2. The corrected H_{DR} swath largely outperforms the conventional H_{DR} swath for nearly all hail size thresholds, confirming that the benefit derived from HailTrack modeling is insensitive to the specific threshold chosen in this case. The optimum thresholds for the conventional swath and corrected swath are identical (37 mm), but the corrected swath has a significantly higher optimum CSI score (0.47 vs 0.37 for the conventional swath). Note also that the skill score improvements noted between conventional and HailTrack-derived MESH swaths also persist across the full range of possible hail size thresholds (not shown). This is relevant to regions without polarimetric radar coverage where the H_{DR} retrieval method cannot be applied.

Having demonstrated that the HailTrack H_{DR} method provides the best correlation to insurance damage, the corresponding maximum hail size and kinetic energy swaths are provided in Fig. 3. The maximum hail size swath shows a period of weak multicell convection to the southwest of Jimboomba with patchy, short-lived hailfall. There are also two contiguous hailstreaks from separate storms that followed a northerly path through the town of Fernvale and the city of Brisbane. These swaths retain spatial continuity despite the discrete temporal nature of the underlying radar data, which is a result of simulating hailstone trajectories from all elevations and from a range of radar volumes. The accumulated kinetic energy swath in Fig. 3b also highlights a smaller region of particularly intense hailfall, which in this case does not match precisely with where the maximally sized hail fell (refer to Fig. 3a). This is a valuable insight, and one that is particularly notable when considering
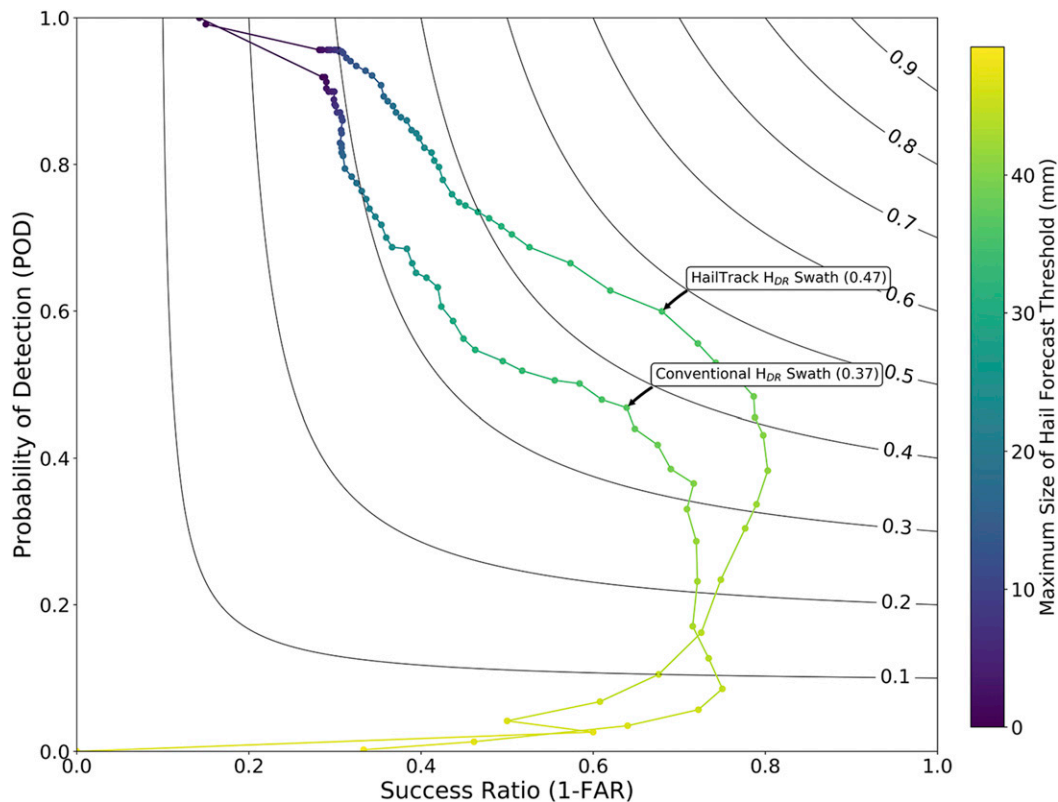
FIG. 2. A Roebber performance diagram for the conventional H_{DR} maximum hail size swath and the HailTrack H_{DR} hail size swath. Each method has a separate line on the plot, and each dot represents a separate threshold for that method (refer to the color bar for threshold values). CSI skill scores are contoured and labeled in black, and the point with the highest CSI value for each method is annotated.

that maximum hail diameter estimations are commonly used as the sole indicator for hailfall intensity in radar-based hail detection methods. It is important to note that only one hailstone is simulated for each H_{DR} radar voxel, and that the true kinetic energy distribution is likely heavily influenced by the size distribution and number concentration of large hail within individual voxels. Accordingly, the KE_H estimates defined here should only be interpreted as a *relative* measure of hailfall intensity. The HailTrack H_{DR} verification scores reported in Table 1 detail how a simple threshold can be used to accurately predict regions experiencing hail damage; however, this provides little information on the accuracy of the actual hail sizes predicted by the hail size swath. To this end, hail reports from the Australian Bureau of Meteorology's severe storms archive for the event are also included in Fig. 3.

There is close (<5-mm difference) agreement between hail size reports in the 30–50 mm range and the corresponding hail swath values in Fig. 3. However, the remaining 70-mm hail report is underestimated by the model with a size prediction of around 50 mm. This is a result of the H_{DR}–d_{hdr} relationship in Eq. (1) underestimating the prevalence of giant hail for this case. The H_{DR} relationship was developed using only 86 hail reports from 12 storms in the United States between 2001 and 2003. The dataset contained only two reports greater than 55 mm in diameter; as a result, the

relationship is undercalibrated for giant hail size predictions. The ability of H_{DR} to estimate giant hail sizes is further hindered by noting it is largely based on horizontal reflectivity. The Z_H alone is useful for discerning small from large hail but shows limited skill for discriminating between large and giant hail because of non-Rayleigh scattering effects (Blair et al. 2011; Ryzhkov et al. 2013b; Ryzhkov and Zrnić 2019). Note also that the maximum MESH value of 76 mm more accurately predicted the maximum reported hail size for this storm (~70 mm). However, unlike previous radar-based hail detection studies, the aim here is to produce a method that predicts the areal extent and intensity of hailfall at the surface, not just the maximum size of hail within a storm's spatiotemporal bounds. This justifies the use of the H_{DR} method for the remaining analysis despite the aforementioned limitations in estimating giant hail sizes. The radar-based methods for estimating hail sizes aloft introduce a considerable amount of uncertainty within the model, as seen in the variations of optimal hail size thresholds in Table 1. Furthermore, as subsequent methods improve hail size estimates in the future, they should be substituted for the current hail retrieval methods used in this study. Any improvements to the specification of hail sizes aloft should also lead to an improvement in the accuracy of trajectory modeling within HailTrack.
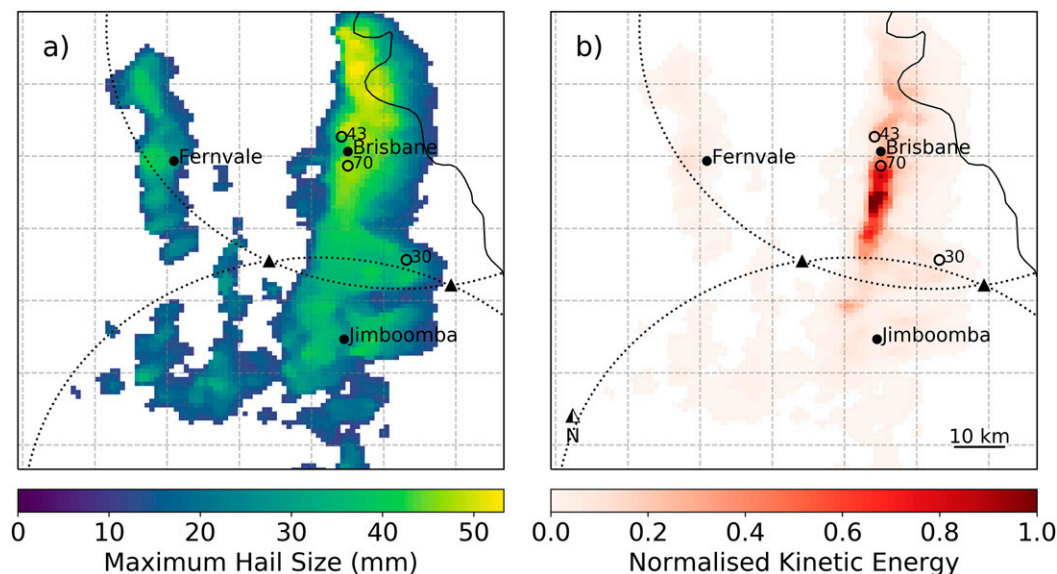
FIG. 3. (a) Accumulated maximum hail size estimates and (b) accumulated hail kinetic energy for the 2014 Brisbane hailstorm using the HailTrack H_{DR} method between 0548 and 0730 UTC. Open circles show the position and size in millimeters of BoM hail reports, and in each panel the filled triangles indicate the positions of radars (CP-2 research radar to the left and the operational Mount Stapylton radar to the right). Dotted lines show dual-Doppler lobes for the 3D wind retrieval with these two radars.

Figure 4 is intended to assist in visualizing the correlation between the HailTrack H_{DR} swaths in Fig. 3 by superimposing them onto hail-related claims. The spatial bounds of Fig. 4 are limited to the main Brisbane hailstreak because there are very little insurance coverage and no hail-related claims outside of this region (due, in part, to lower population density). The spatial extent of hail-related damage is captured well by the hail size contours in Fig. 4a, with the exception of a small amount of hail damage on the western edge of the damage swath. The kinetic energy "hot spot" region also correlates well with the highest hail damage percentages, as shown in Fig. 4b. The southern extent of the kinetic energy contours appears to overestimate the relative hail intensity, although there is a large number of grid points with no insurance data in this region. An attempt was made to quantify the relationship between the predicted and observed hail intensities. A point-matched linear regression between the accumulated kinetic energy field and damage percentage field (not shown) yields an r^2 value of 0.54. This indicates a moderate positive correlation between accumulated kinetic energy and the percentage of contracts with damage claims. There is potential to improve this damage intensity relationship by weighting variables such as diameter or impact velocity, or by introducing new variables such as the impact angle of hailstone impacts as wind-driven hail likely causes more severe damage (e.g., Richter et al. 2014).

Figure 5 further illustrates the improvement in hailfall estimation derived from modeling hail trajectories. The conventional H_{DR} swath in Fig. 5a exhibits a clear spatial offset from the insurance damage swath as hailstones are detected aloft before they are advected westward. Figure 5b shows this spatial offset is mostly removed from the corrected swath as it is well

aligned with the insurance damage swath. This indicates that hailstones predominantly advected toward the west in this case study, and that accounting for this motion significantly improves the correlation with surface damage. Figure 5 also shows that the HailTrack swath is up to 7 km wider than the conventional swath due to the effects of differential hail advection. A more direct discussion of the direction and magnitude of advection within these experiments is provided in section 4. The poorest correlation to hail damage is located on the meridional extremities of the hail swaths. Sensitivity tests (not shown) indicate that decreasing the threshold size would encompass these regions, but it would also result in a higher false alarm rate, especially in regions south of the two radars. It is difficult to assess whether these inaccuracies stem from HailTrack modeling assumptions, initial hail size estimates or the aforementioned observational limitations involved with insurance claims. The sensitivity of the model with respect to microphysical modeling assumptions is discussed in section 5.

4. Trajectory analysis

Figure 6 shows three selected 17-mm hailstones initiated close to the updraft at 0642 UTC during the 2014 Brisbane hailstorm. The initial positions and sizes of these trajectories were chosen to illustrate the effects of assumptions within the model and to demonstrate the importance of trajectory modeling for estimating hail advection. First, trajectory A in Fig. 6 transects the updraft through the lower levels while advecting toward the northwest. This hailstone is partially suspended while traversing the updraft, increasing its residence time below the melting level and allowing it to develop a ∼10% larger meltwater fraction than trajectories B and C. Trajectory A also
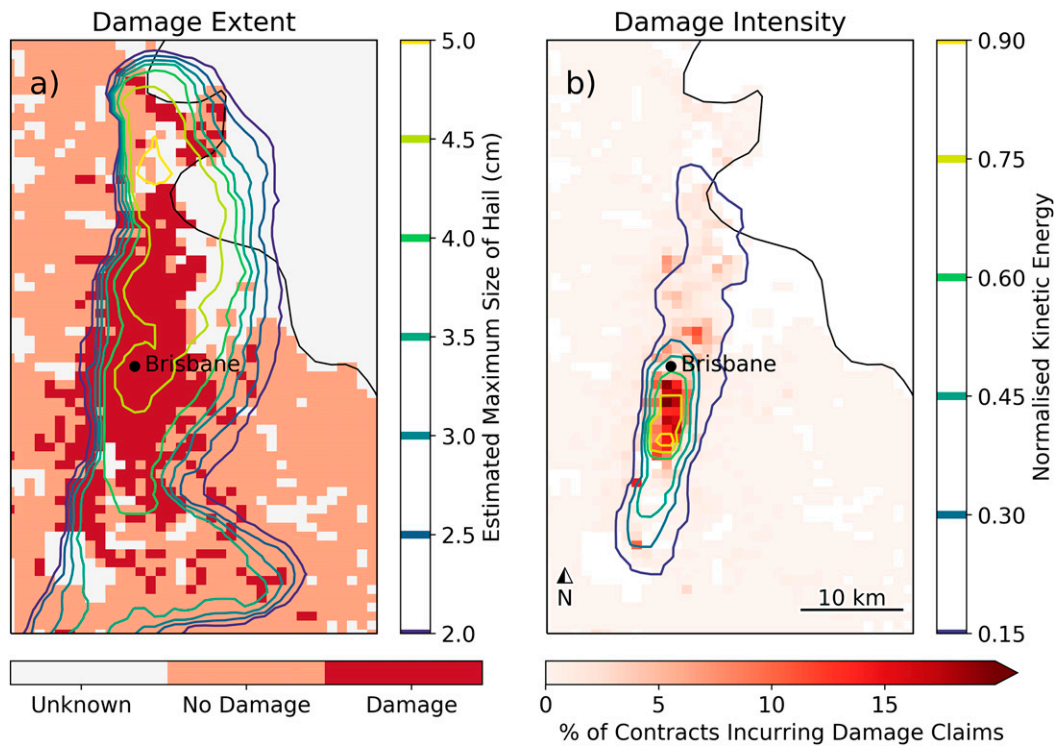
FIG. 4. (a) Contours of the HailTrack H_{DR} accumulated maximum hail size swath plotted over a binary representation of hail damage from the 27 Nov 2014 Brisbane hailstorm. Grid boxes with no insurance data are marked as "unknown," boxes with contracts but no damage claims are indicated as "no damage," and boxes with damage claims are marked as "damage" (shading). (b) Contours of normalized accumulated kinetic energy shown over the percentage of contracts that incurred hail claims.

shows that hailstones initiated at low elevations (2.5-km altitude in this case) may advect considerable distances in the presence of strong low-level winds. Trajectory B is initiated in the updraft at an altitude of 7 km. This hailstone exhibits what is known as a "recycling" trajectory where hailstones are entrained within the updraft on multiple occasions. Hailstone recycling was associated with the growth of large hailstones in some early trajectory studies (e.g., Browning 1963); however, more recent literature indicates these repeated vertical excursions are inhibited by hailstone growth processes (Kumjian and Lombardo (2020) and references therein). The microphysical modeling within HailTrack considers hailstone melting alone, which limits its ability to accurately model trajectories that are strongly affected by hail growth. This limitation highlights that the intended use of HailTrack is to simulate the trajectories and fall out locations of hailstones once they have grown close to their maximum diameter. Equivalently, hailstones that are still undergoing large amounts of growth at the time of radar observation will likely be simulated more accurately in subsequent radar scans.

Trajectory C in Fig. 6 is initiated at an 11-km altitude within the updraft. Strong southwesterly winds associated with updraft divergence advected the hailstone into a downdraft region roughly 5 km to the east. Here, the hailstone descends sharply before encountering the low-level southeasterly winds also observed in trajectory A. This analysis indicates that the

horizontal wind profile in the updraft region is veering strongly with increased height. The resulting hailstone impact locations are separated by up to 8 km along the x axis, despite all having been initiated along the center of the updraft ($x = \sim 12$ km). These disparate advection magnitudes occurred on both sides of the storm, perpendicular to the northerly bulk storm motion. To further quantify the magnitude and direction of hailstone advection within this case study, the difference between the initial and final hailstone positions during the HailTrack H_{DR} model run is shown in Fig. 7. The model predicts that small hailstones can advect large distances greater than 9 km. Figure 7 also shows that large hailstones capable of damaging buildings and structures can advect up to 6 km away from their initial locations aloft. These results provide evidence of size sorting within the model as wind forcing has a disparate effect on hailstones depending on their size. Sorting causes a gradient in hail diameters across hail swaths and this has been observed in a range of observational and modeling studies (Ryzhkov et al. 2005; Kumjian and Ryzhkov 2008, 2012; Dawson et al. 2014). The broad distribution of advection vectors within size classes also indicates that advection is heavily dependent on the spatiotemporal path taken by the hailstones through the 3D wind field. Advection in this storm occurs predominantly in a northwesterly direction relative to the surface. There is very little advection toward the south, consistent with the overall northerly storm motion.
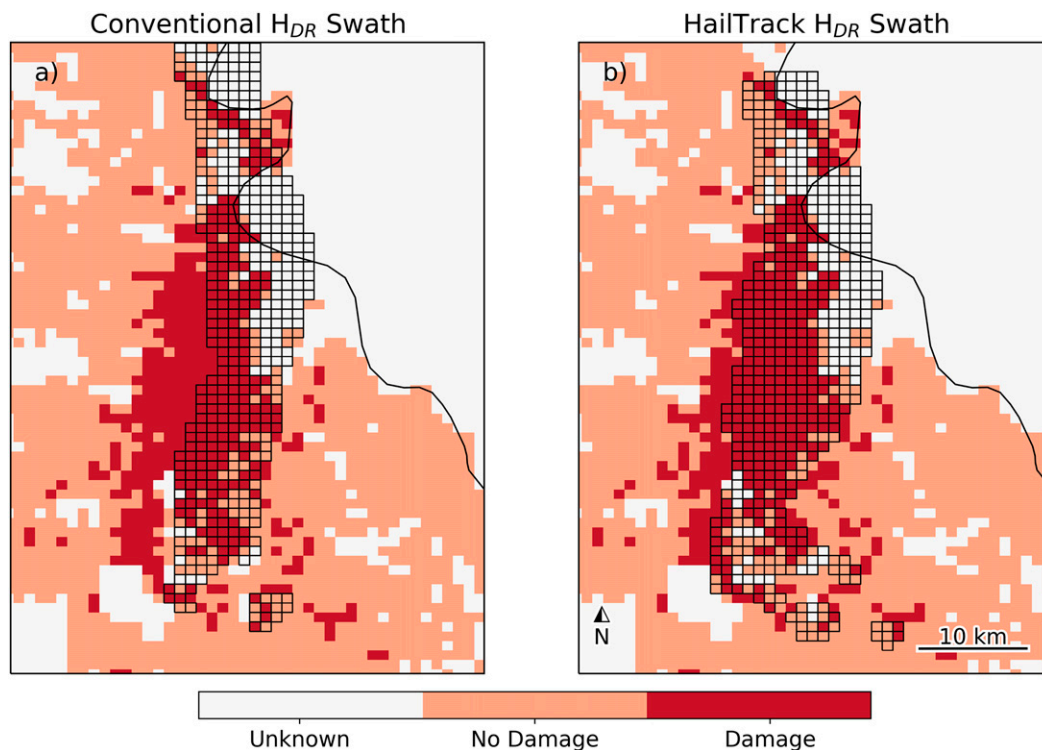
Conventional H_{DR} Swath   HailTrack H_{DR} Swath

FIG. 5. (a) A binary representation of insurance damage as in Fig. 4 overlaid with a grid of outlined cells containing conventional H_{DR} swath values greater than the optimum 37-mm threshold. (b) As in (a), but using the HailTrack H_{DR} swath.

Many previous studies have used a stormwide correction vector to account for hail advection (Schiesser 1990; Schmid et al. 1992; Hohl et al. 2002; Schuster et al. 2006). Here, such a correction is approximated for comparison purposes by finding the average of each individual advection vector shown in Fig. 7. The resulting vector has a 2100 m magnitude and a bearing of N 30° W. To assess the accuracy of this simple horizontal shift method, the conventional H_{DR} swath shown in Fig. 5a was shifted according to the average advection vector. The shifted swath produced a HSS of 0.52 when compared with insurance validation data, which is a modest improvement over the conventional H_{DR} method (HSS = 0.48). The improvements gained through the simple horizontal shift method are considerably less than what are achieved through the trajectory modeling approach introduced here (HSS = 0.58). This is largely because hail advection may not be accurately characterized by a single spatial offset vector, owing to the overall diversity of advection vectors (refer to Fig. 7). An inhomogeneous set of advection vectors effectively widens the resulting hail swath on both edges of the storm, as illustrated by the comparison of conventional and HailTrack swaths in Fig. 5. Put concisely, the HailTrack method improves hailfall estimation through a combination of both horizontal shifting and widening of conventional swaths in this case.

The average advection vector calculated above indicates that hail advected approximately 30° to the left of the northerly bulk storm motion. Previous studies have attempted to draw a causal relationship between the underlying storm dynamics

and the resulting hail advection direction (Schiesser 1990; Schmid et al. 1992; Schuster et al. 2006). These explanations depend on storms exhibiting a quasi-stationary, supercellular structure where storm dynamics are well understood. The storm investigated here is categorized well by Nelson (1987) as a hybrid multicell–supercell storm; evidenced by a large elevated hail core (high reflectivity > 65 dBZ; differential reflectivity < 0 dB), concurrent bounded weak echo regions and multiple short-lived velocity couplets throughout the lifetime of the storm (Soderholm et al. 2017). This structural classification precludes any robust, qualitative comparison to previous storm dynamics literature. Such an analysis is also complicated by the difficulties involved with accurately characterizing the full set of advection vectors shown in Fig. 7 with a single "average" advection direction.

Another novel aspect of the trajectory model in this study is the ability to investigate the impact angle of hailstones. Impact angles are defined as the angle between the hailstone's impact velocity vector and the vertical. Figure 8 shows the distributions of impact angles within HSDA size categories. Hailstones that encountered gaps in the wind field (see section 2c) are excluded from this figure. This was done to ensure the impact angles presented result from interactions with direct wind field retrievals and not gap-filled estimates. Both the mean and standard deviation of the approximately Gaussian distribution of impact angles decrease with increasing hail size. This is due to the terminal velocities of large hailstones having a more significant influence on impact velocity vectors. The
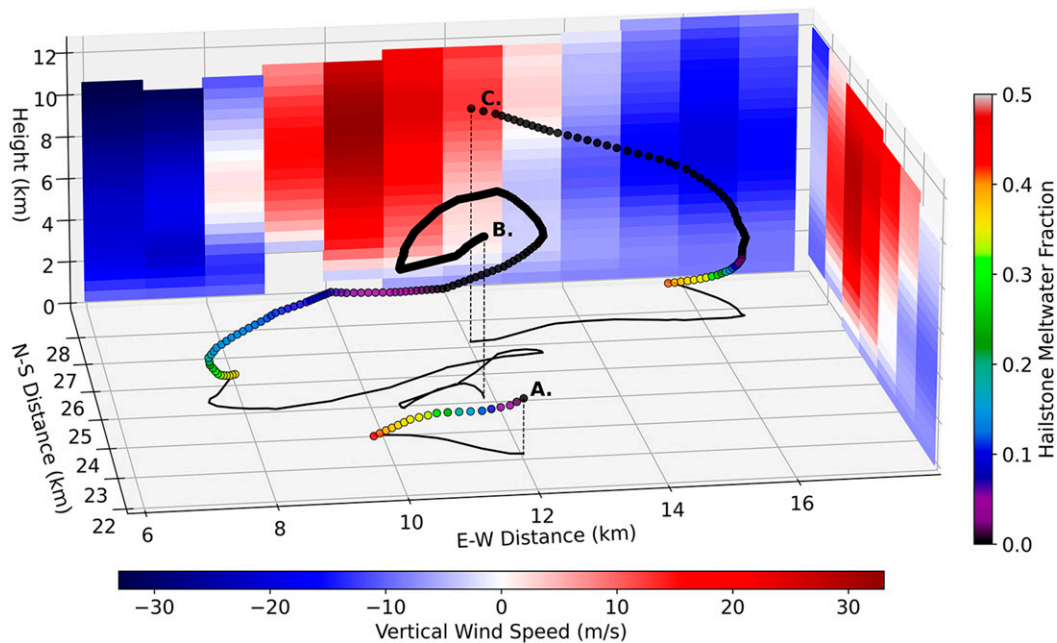
FIG. 6. Trajectories of three 17-mm hailstones inserted along the center of the updraft region for the 2014 Brisbane hailstorm at 0642 UTC. Cross sections of vertical wind speed are taken at $x = 12$ km and $y = 25$ km to assist in relating hail trajectories to the underlying storm dynamics. Filled circles represent hailstone positions at each 10-s trajectory step and are shaded according to meltwater fraction to illustrate the melting process. Solid lines represent a 2D projection of hailstone trajectories onto the surface of the model grid, with dotted lines linking the initial position of hailstones to their corresponding projection.

importance of hail impact angles is noted in studies based on building damage due to hail (Hohl et al. 2002; Brown et al. 2015). Low impact angles limit hail damage to mostly roofing, whereas high impact angles increase the potential for siding and window damage to structures. Furthermore, large horizontal velocity components associated with high impact angles increase the magnitude of the total impact velocity. The addition of horizontal velocity components in this study increased the average estimated impact velocities by 22%; however, this is highly weighted by smaller sizes due to their prevalence in the model. Discriminating into HSDA size categories reveals that the addition of horizontal velocities increases the average impact magnitude by 24% for small hailstones, 17% for large hailstones, and only 4% for giant hailstones. To the authors' knowledge, no observational studies have investigated the impact angles of natural hail, preventing a comparison of these results to existing literature. This, along with the aforementioned problems involved with retrieving low-level wind fields from radar data limit the confidence level for the results shown in Fig. 8. Nevertheless, we have included these results as a step toward more accurately estimating the potential impacts of hail in the presence of strong low-level winds using remote sensing methods.

In addition to mapping hailfall for historical events, the forward trajectory approach used here can also be applied to generate short-term predictions of hailfall. The lead time of these nowcasts is reliant on both the simulated trajectory durations and the computational efficiency of the model. For a

10-s trajectory time step ($\Delta t = 10$ s), the current software implementation of HailTrack processes an operational radar volume ($>10\,000$ trajectories in this case) in less than 20 s, making it suitable for nowcasting without the need for parallel processing. An example nowcast created using the HailTrack H_{DR} method for the Brisbane 2014 hailstorm is given in Fig. 9. This nowcast incorporates all radar volumes up to 0642 UTC and is intended to be successively updated with trajectories from new radar volumes during an event. This figure illustrates the immediate hail risk with a maximum of roughly 10–15-min lead time. Each point on the figure represents a hail impact, with colors indicating the expected time until impact and point sizes varying proportionally to impact diameters. Although the lead time of such a nowcast may be too short for most conventional nowcasting applications, the specificity of these warnings may reduce the number of false alarms commonly associated with hail nowcasts. The trajectory model can therefore potentially assist decision-making around hail risk in the minutes leading up to hail events.

5. Sensitivity experiments

To test the sensitivity of the model to microphysical modeling assumptions, five additional H_{DR}-based simulations were performed. These five experiments are compared to the default HailTrack H_{DR} model runs presented so far, which initiated size-dependent hailstone densities based on Eq. 4 and sourced thermodynamic variables directly from a representative
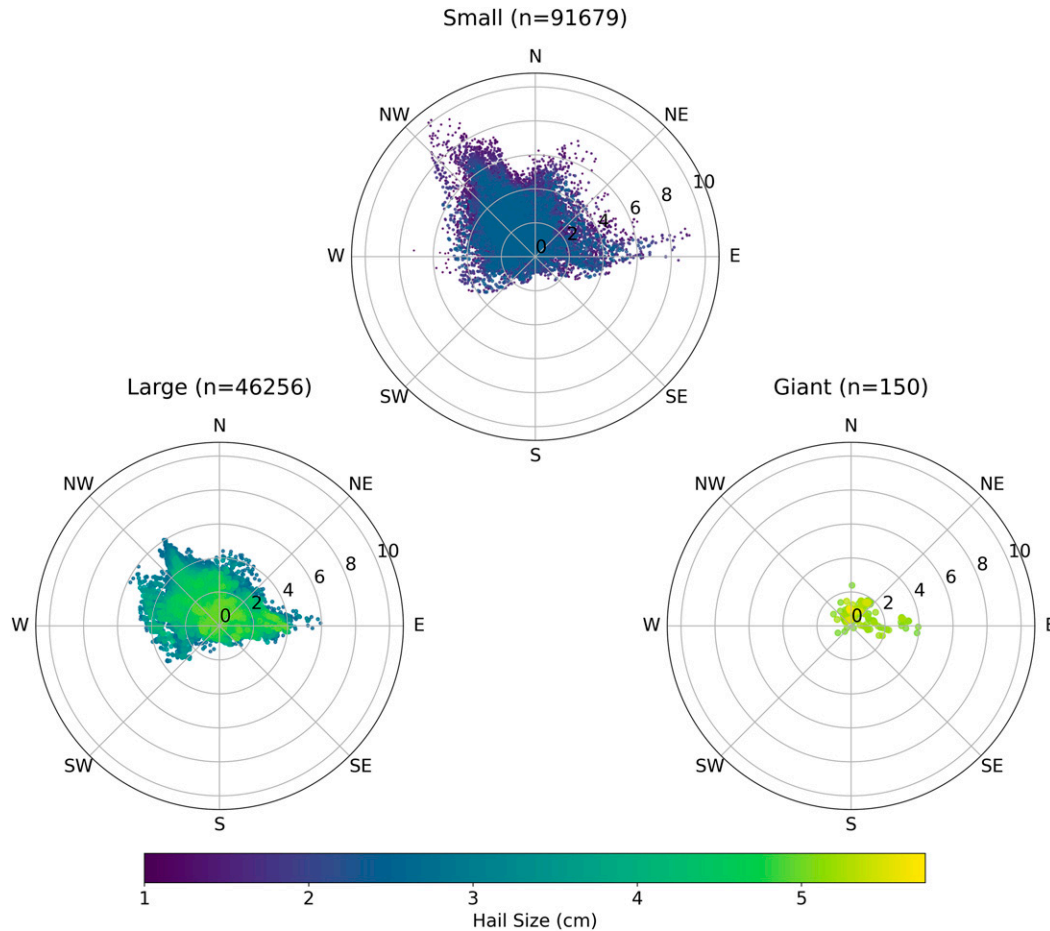
FIG. 7. Hail advection calculated by the difference between the initial and final horizontal position of each modeled hailstone initiated using the HailTrack H_{DR} method. Advection plots are split between HSDA hail size categories, with the number of hailstones in each category shown in the title. Radial labels represent the advection magnitude in kilometers. Individual hailstone points are colored and plotted in order of their sizes.

sounding. The sounding indicates that the 0°C isotherm was located at an altitude of 3900 m, with an approximately constant temperature lapse rate of 6.9 K km^{-1} beneath. The five additional sensitivity experiments are named as follows: "spongy" (initial hailstone densities set similar to that of graupel, 600 kg m^{-3}), "solid" (initial hailstone densities set to that of solid ice, 917 kg m^{-3}), "hot" (10°C offset added to the entire temperature profile), "cold" (−10°C offset added to the entire temperature profile), and "no melt" (melting model switched off within code). Note that the environmental relative humidity profiles were held constant in the hot and cold experiments. Notable properties for each of these experiments are reported in Table 2.

The maximum change in diameter due to melting in the default experiment was 12 mm, resulting in a minimum hail size of 5 mm at the surface. This indicates that even hailstones that experience favorable melting trajectories (partial suspension by the updraft beneath the melting layer; e.g., trajectory A in Fig. 6), do not melt completely with default settings in this case study. Complete hailstone melting was observed in the spongy

and hot experiments, results that are easily understood as a combination of decreased ice mass and terminal velocity for low density hail, and enhanced heat transfer for the hotter environmental profile. The effects of enhanced melting also translate to the impact estimates reported in Table 2. Enhanced hailstone melting lowered the maximum impact velocity and kinetic energy of hailstones within the additional experiments, relative to the corresponding 43.5 m s^{-1} and 54.8-J values for the default experiment, respectively. Microphysical changes can also potentially affect the accuracy of hail swaths by altering the amount of advection experienced by hailstones. Table 2 shows that the low density, spongy experiment exhibited considerably larger average and maximum advection magnitudes due to the accompanying reductions in terminal velocity. Changes in advection magnitudes in the other sensitivity experiments are less pronounced, indicating that changes in hailstone size and terminal velocities due to melting do not significantly alter advection magnitudes in those cases.

Impact estimates created using the H_{DR} method, along with default microphysical settings achieved a HSS of 0.58. The
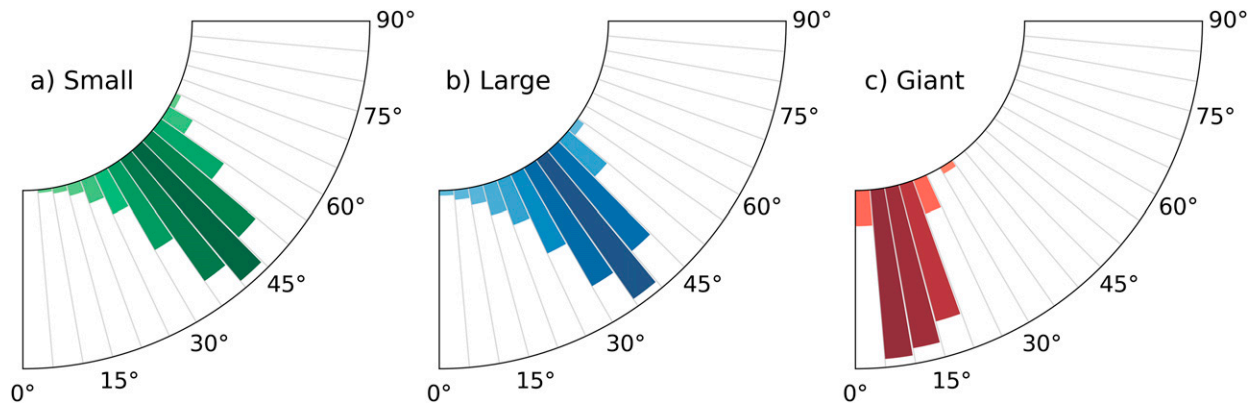
FIG. 8. Frequency histograms for impact angles of the three HSDA hail size categories for all modeled hailstones using the HailTrack H_{DR} method. Impact angles are measured as the angle between the impact velocity vector and the surface normal vector. An impact angle of 0° indicates a perpendicular impact relative to the surface.

damage prediction skill for the remaining experiments is similar (0.58 ± 0.01) despite the microphysical changes, as the optimum hail size threshold adjusted according to the amount of melting. This indicates that the observed increase in skill scores relative to the conventional H_{DR} method is predominantly the result of modeling hail advection and not hail melting in this case. However, the observed variability in optimal thresholds for each of the sensitivity experiments does

have a physical significance. The model is ultimately accounting for the fact that hailfall intensity metrics (e.g., maximum size and kinetic energy) can change between the observation aloft and verification at the surface (e.g., using a hail size report). When verifying conventional methods, these postobservation melting effects are not explicitly accounted for, and this additional variability is then introduced into relationships between remotely sensed observations and surface
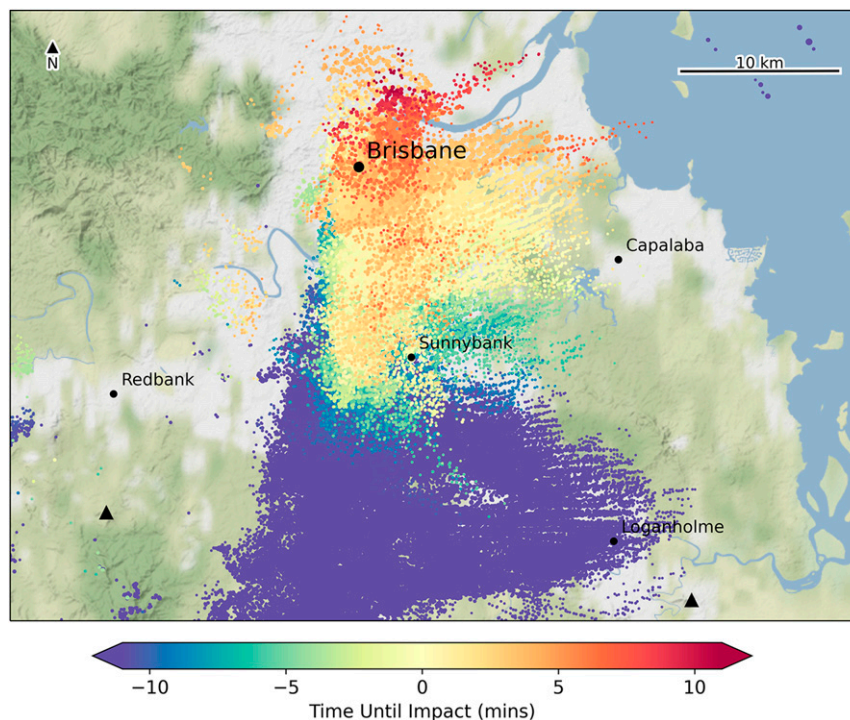

FIG. 9. An example of a potential nowcast from HailTrack calculated using all H_{DR} hail size retrievals before the 0642 UTC radar scan. Points on the map indicate the position of modeled hail impacts; these are shaded according to the time in minutes until hail impact plotted in ascending order. Negative numbers indicate hail that has already fallen before 0642 UTC, and positive numbers show how long after 0642 UTC hail that is currently aloft is expected to land.

TABLE 2. Results of microphysical sensitivity tests; refer to the text for a description of the model settings for each experiment. Various parameters of interest are shown for each model setting and are discussed within the text.

Expt	Default	Spongy	Solid	Hot	Cold	No Melt
Min diameter (mm)	5	0	5	0	14	17
Max diameter (mm)	58	49	58	54	60	61
Max melt (mm)	12	17	12	21	3	0
Max velocity (m s^{-1})	43.5	40.4	43.5	43.5	42.5	43.5
Max KE (J)	54.8	17.7	54.8	43.6	61.6	63.2
Avg advection (m)	2100	2600	2100	2200	2200	2100
Max advection (m)	10 100	13 600	9300	10 300	10 500	10 100
Threshold (mm)	37.2	31.5	37.2	34.7	39.6	40.4
Swath area (km^2)	557	555	551	518	535	523
HSS	0.58	0.58	0.59	0.58	0.57	0.58

validation data. The significance of accounting for these effects will become clear when attempting to find a consistent, optimum hail size threshold between events with disparate thermodynamic environments or hail density distributions aloft, as this postobservation variability will be partially alleviated through the use of the melting model. Additional high-resolution insurance validation datasets for severe hailstorms will enable this testing in the future.

6. Summary and future directions

This study introduced HailTrack, a novel method aimed at improving radar-based hail impact estimates. Radar retrievals were used to estimate hail size and position aloft, before trajectory simulations were run to predict where hailstones will impact the ground. Three radar-based hail size retrievals (MESH, H_{DR}, and HSDA) were tested to initiate trajectories and a dual-Doppler, three-dimensional wind field was used to model hailstone advection. A thermodynamic melting model was also coupled with trajectory simulations to reflect the changing size and terminal velocities of hailstones below the melting level.

We applied the model to a case study in Brisbane that produced >70-mm hail and over AUD 1.5 billion in insured losses. Hail-related insurance claims were used to verify the model, and this analysis concluded that HailTrack-derived swaths significantly outperformed the corresponding conventional swaths. Further, the H_{DR} hail retrieval method was found to produce the most accurate results. A 37-mm hail size threshold optimized the correlation between H_{DR} swaths and insurance damage, and the relative improvement of HailTrack swaths (HSS = 0.58) over conventional swaths (HSS = 0.48) was found to be insensitive to the specific choice of this threshold. Kinetic energy accumulations of hail impacts also showed a moderate linear correlation with the percentage of insurance contracts that experienced hail damage.

Trajectory analysis in section 4 concluded that hailstones may advect up to 10 km away from their initial positions aloft due to strong winds in hail producing regions of the storm. Smaller hailstones were shown to advect farther and impact more horizontally than larger hailstones due to their smaller terminal velocities. Hailstone advection in this storm occurred predominantly in a northwesterly cardinal direction, ~40° to the left of the bulk storm motion vector with an average magnitude of 2100 m. Horizontally shifting conventional swaths by this average advection vector improved the correlation to insurance data by partially accounting for advection. However, this improvement was considerably less than that obtained by HailTrack, which can be attributed to the new method's ability to model the full complexity of hail advection. The potential to produce a forward trajectory-based nowcast in real time during hail events was also introduced and was noted to produce lead times of around 10–15 min in this case.

Future work should involve extending the model validation in this study to a larger sample size of hail events to more robustly quantify the improvements obtained through the use of HailTrack. This research is currently limited by a lack of ground-truth data, which highlights the need for improved hail observations and further collaboration with the insurance industry. In the future, we aim to extend the lead time of HailTrack nowcasts by applying the model to storms advected forward in time or by adding an existing parameterization of hail growth (e.g., Paluch 1978; Ziegler et al. 1983). Further investigations should also quantify how rapid-scan radar data could improve the existing implementation of HailTrack by more accurately estimating the temporal evolution of wind dynamics and the hail distribution aloft. Last, the applicability of the trajectory modeling approach could be greatly improved by removing the requirement for dual-Doppler radar coverage. To this end, future studies should investigate the accuracy of hail trajectories calculated using 3D, single-Doppler wind retrievals (e.g., Gao et al. 2006; Potvin and Wicker 2012).

Data availability statement. Public access to the insurance dataset used in this study is restricted because of data disclosure agreements with Suncorp Insurance. All radiosonde, radar, and

3D wind data have been made available online (https://doi.org/10.5281/zenodo.3600107).

REFERENCES

Allen, J. T., and E. R. Allen, 2016: A review of severe thunderstorms in Australia. *Atmos. Res.*, **178–179**, 347–366, https://doi.org/10.1016/j.atmosres.2016.03.011.

——, M. K. Tippett, W. S. Ashley, M. R. Kumjian, and D. Cavanaugh, 2015: The characteristics of United States hail reports: 1955-2014. *Electron. J. Severe Storms Meteor.*, **10** (3), http://www.ejssm.org/ojs/index.php/ejssm/article/viewArticle/149.

Auer, A. H., and J. D. Marwitz, 1972: Hail in the vicinity of organized updrafts. *J. Appl. Meteor.*, **11**, 748–752, https://doi.org/10.1175/1520-0450(1972)011<0748:HITVOO>2.0.CO;2.

Aydin, K., T. A. Seliga, and V. Balaji, 1986: Remote sensing of hail with a dual linear polarization radar. *J. Climate Appl. Meteor.*, **25**, 1475–1484, https://doi.org/10.1175/1520-0450(1986)025<1475:RSOHWA>2.0.CO;2.

Barnes, S. L., 1964: A technique for maximizing details in numerical weather map analysis. *J. Appl. Meteor.*, **3**, 396–409, https://doi.org/10.1175/1520-0450(1964)003<0396:ATFMDI>2.0.CO;2.

Basara, J. B., D. R. Cheresnick, D. Mitchell, and B. G. Illston, 2007: An analysis of severe hail swaths in the southern plains of the United States. *Trans. GIS*, **11**, 531–554, https://doi.org/10.1111/j.1467-9671.2007.01059.x.

Blair, S., D. R. Deroche, J. M. Boustead, J. W. Leighton, B. L. Barjenbruch, and W. P. Gargan, 2011: A radar-based assessment of the detectability of giant hail. *Electron. J. Severe Storms Meteor.*, **6** (7), https://www.ejssm.org/ojs/index.php/ejssm/article/viewArticle/87.

Brown, T. M., W. H. Pogorzelski, and I. M. Giammanco, 2015: Evaluating hail damage using property insurance claims data. *Wea. Climate Soc.*, **7**, 197–210, https://doi.org/10.1175/WCAS-D-15-0011.1.

Browning, K. A., 1963: The growth of large hail within a steady updraught. *Quart. J. Roy. Meteor. Soc.*, **89**, 490–506, https://doi.org/10.1002/qj.49708938206.

Changnon, S. A., 1968: Effect of sampling density on areal extent of damaging hail. *J. Appl. Meteor.*, **7**, 518–521, https://doi.org/10.1175/1520-0450(1968)007<0518:EOSDOA>2.0.CO;2.

——, 1970: Hailstreaks. *J. Atmos. Sci.*, **27**, 109–125, https://doi.org/10.1175/1520-0469(1970)027<0109:H>2.0.CO;2.

Cintineo, J. L., T. M. Smith, V. Lakshmanan, H. E. Brooks, and K. L. Ortega, 2012: An objective high-resolution hail climatology of the contiguous United States. *Wea. Forecasting*, **27**, 1235–1248, https://doi.org/10.1175/WAF-D-11-00151.1.

Collis, S., A. Protat, P. T. May, and C. Williams, 2013: Statistics of storm updraft velocities from TWP-ICE including verification with profiling measurements. *J. Appl. Meteor. Climatol.*, **52**, 1909–1922, https://doi.org/10.1175/JAMC-D-12-0230.1.

Conway, J. W., and D. S. Zrnić, 1993: A study of embryo production and hail growth using dual-Doppler and multiparameter radars. *Mon. Wea. Rev.*, **121**, 2511–2528, https://doi.org/10.1175/1520-0493(1993)121<2511:ASOEPA>2.0.CO;2.

Dawson, D. T., E. R. Mansell, Y. Jung, L. J. Wicker, M. R. Kumjian, and M. Xue, 2014: Low-level Z_{DR} signatures in supercell forward flanks: The role of size sorting and melting of hail. *J. Atmos. Sci.*, **71**, 276–299, https://doi.org/10.1175/JAS-D-13-0118.1.

Depue, T. K., P. C. Kennedy, and S. A. Rutledge, 2007: Performance of the hail differential reflectivity (H_{DR}) polarimetric radar hail indicator. *J. Appl. Meteor. Climatol.*, **46**, 1290–1301, https://doi.org/10.1175/JAM2529.1.

Dixon, M., and G. Wiener, 1993: TITAN: Thunderstorm Identification, Tracking, Analysis, and Nowcasting—A radar-based methodology. *J. Atmos. Oceanic Technol.*, **10**, 785–797, https://doi.org/10.1175/1520-0426(1993)010<0785:TTITAA>2.0.CO;2.

Dolan, B., and S. A. Rutledge, 2009: A theory-based hydrometeor identification algorithm for X-band polarimetric radars. *J. Atmos. Oceanic Technol.*, **26**, 2071–2088, https://doi.org/10.1175/2009JTECHA1208.1.

——, ——, S. Lim, V. Chandrasekar, and M. Thurai, 2013: A robust C-band hydrometeor identification algorithm and application to a long-term polarimetric radar dataset. *J. Appl. Meteor. Climatol.*, **52**, 2162–2186, https://doi.org/10.1175/JAMC-D-12-0275.1.

Doswell, C. A., R. Davies-Jones, and D. L. Keller, 1990: On summary measures of skill in rare event forecasting based on contingency tables. *Wea. Forecasting*, **5**, 576–585, https://doi.org/10.1175/1520-0434(1990)005<0576:OSMOSI>2.0.CO;2.

Fraile, R., J. L. Sánchez, J. L. de la Madrid, A. Castro, and J. L. Marcos, 1999: Some results from the hailpad network in León (Spain): Noteworthy correlations among hailfall parameters. *Theor. Appl. Climatol.*, **64**, 105–117, https://doi.org/10.1007/s007040050115.

Gao, J., M. Xue, S.-Y. Lee, A. Shapiro, Q. Xu, and K. Droegemeier, 2006: A three-dimensional variational single-Doppler velocity retrieval method with simple conservation equation constraint. *Meteor. Atmos. Phys.*, **94**, 11–26, https://doi.org/10.1007/s00703-005-0170-7.

Greene, D. R., and R. A. Clark, 1972: Vertically integrated liquid water—A new analysis tool. *Mon. Wea. Rev.*, **100**, 548–552, https://doi.org/10.1175/1520-0493(1972)100<0548:VILWNA>2.3.CO;2.

Heidke, P., 1926: Berechnung des Erfolges und der Güte der Windstärkevorhersagen im Sturmwarnungsdienst. *Geogr. Ann.*, **8**, 301–349, https://doi.org/10.1080/20014422.1926.11881138.

Helmus, J. J., and S. M. Collis, 2016: The Python Arm Radar Toolkit (Py-ART), a library for working with weather radar data in the python programming language. *J. Open Res. Software*, **4**, e25, https://doi.org/10.5334/jors.119.

Hohl, R., H.-H. Schiesser, and D. Aller, 2002: Hailfall: The relationship between radar-derived hail kinetic energy and hail damage to buildings. *Atmos. Res.*, **63**, 177–207, https://doi.org/10.1016/S0169-8095(02)00059-5.

Insurance Council of Australia, 2017: ICA catastrophe database. Insurance Council of Australia, accessed 4 April 2020, https://www.icadataglobe.com/dataglobeposts/accessicadata.

Jewell, R., and J. Brimelow, 2009: Evaluation of Alberta hail growth model using severe hail proximity soundings from the United States. *Wea. Forecasting*, **24**, 1592–1609, https://doi.org/10.1175/2009WAF2222230.1.

Jin, H.-G., H. Lee, J. Lkhamjav, and J.-J. Baik, 2017: A hail climatology in South Korea. *Atmos. Res.*, **188**, 90–99, https://doi.org/10.1016/j.atmosres.2016.12.013.

Kahraman, A., S. Tilev-Tanriover, M. Kadioglu, D. M. Schultz, and P. M. Markowski, 2016: Severe hail climatology of Turkey. *Mon. Wea. Rev.*, **144**, 337–346, https://doi.org/10.1175/MWR-D-15-0337.1.

Kumjian, M. R., and A. V. Ryzhkov, 2008: Polarimetric signatures in supercell thunderstorms. *J. Appl. Meteor. Climatol.*, **47**, 1940–1961, https://doi.org/10.1175/2007JAMC1874.1.

——, and ——, 2012: The impact of size sorting on the polarimetric radar variables. *J. Atmos. Sci.*, **69**, 2042–2060, https://doi.org/10.1175/JAS-D-11-0125.1.

——, and K. Lombardo, 2020: A hail growth trajectory model for exploring the environmental controls on hail size: Model

physics and idealized tests. *J. Atmos. Sci.*, **77**, 2765–2791, https://doi.org/10.1175/JAS-D-20-0016.1.

Kunz, M., and M. Puskeiler, 2010: High-resolution assessment of the hail hazard over complex terrain from radar and insurance data. *Meteor. Z.*, **19**, 427–439, https://doi.org/10.1127/0941-2948/2010/0452.

Lakshmanan, V., K. Hondl, and R. Rabin, 2009: An efficient, general-purpose technique for identifying storm cells in geospatial images. *J. Atmos. Oceanic Technol.*, **26**, 523–537, https://doi.org/10.1175/2008JTECHA1153.1.

——, M. Miller, and T. Smith, 2013: Quality control of accumulated fields by applying spatial and temporal constraints. *J. Atmos. Oceanic Technol.*, **30**, 745–758, https://doi.org/10.1175/JTECH-D-12-00128.1.

Marshall, T. P., R. F. Herzog, S. J. Morrison, and S. R. Smith, 2002: Hail damage threshold sizes for common roofing materials. *21st Conf. on Severe Local Storms*, San Antonio, TX, Amer. Meteor. Soc., P3.2, https://ams.confex.com/ams/pdfpapers/45858.pdf.

Murillo, E. M., and C. R. Homeyer, 2019: Severe hail fall and hailstorm detection using remote sensing observations. *J. Appl. Meteor. Climatol.*, **58**, 947–970, https://doi.org/10.1175/JAMC-D-18-0247.1.

Nanni, S., P. Mezzasalma, and P. P. Alberoni, 2000: Detection of hail by means of polarimetric radar data and hailpads: Results from four storms. *Meteor. Appl.*, **7**, 121–128, https://doi.org/10.1017/S135048270000147X.

Nelson, S. P., 1987: The hybrid multicellular–supercellular storm—An efficient hail producer. Part II. General characteristics and implications for hail growth. *J. Atmos. Sci.*, **44**, 2060–2073, https://doi.org/10.1175/1520-0469(1987)044<2060:THMSEH>2.0.CO;2.

Ortega, K. L., 2018: Evaluating multi-radar, multi-sensor products for surface hailfall diagnosis. *Electron. J. Severe Storms Meteor.*, **13** (1), https://ejssm.org/ojs/index.php/ejssm/article/viewArticle/163.

——, T. M. Smith, K. L. Manross, K. A. Scharfenberg, A. Witt, A. G. Kolodziej, and J. J. Gourley, 2009: The Severe Hazards Analysis and Verification Experiment. *Bull. Amer. Meteor. Soc.*, **90**, 1519–1530, https://doi.org/10.1175/2009BAMS2815.1.

——, J. M. Krause, and A. V. Ryzhkov, 2016: Polarimetric radar characteristics of melting hail. Part III: Validation of the algorithm for hail size discrimination. *J. Appl. Meteor. Climatol.*, **55**, 829–848, https://doi.org/10.1175/JAMC-D-15-0203.1.

Paluch, I. R., 1978: Size sorting of hail in a three-dimensional updraft and implications for hail suppression. *J. Appl. Meteor.*, **17**, 763–777, https://doi.org/10.1175/1520-0450(1978)017<0763:SSOHIA>2.0.CO;2.

Parackal, K. I., M. S. Mason, D. J. Henderson, D. J. Smith, and J. D. Ginger, 2015: Investigation of damage: Brisbane 27 November 2014 severe storm event. *Research proceedings from the 2015 bushfire and natural hazards CRC and AFAC conference*, M. Rumsewicz, Ed., Bushfire and Natural Hazards CRC, 240–248, https://www.bnhcrc.com.au/publications/researchproceedings2015.

Park, H. S., A. V. Ryzhkov, D. S. Zrnić, and K.-E. Kim, 2009: The hydrometeor classification algorithm for the polarimetric WSR-88D: Description and application to an MCS. *Wea. Forecasting*, **24**, 730–748, https://doi.org/10.1175/2008WAF2222205.1.

Potvin, C. K., and L. J. Wicker, 2012: Comparison between dual-Doppler and EnKF storm-scale wind analyses: Observing system simulation experiments with a supercell thunderstorm.

Mon. Wea. Rev., **140**, 3972–3991, https://doi.org/10.1175/MWR-D-12-00044.1.

Protat, A., and I. Zawadzki, 1999: A variational method for real-time retrieval of three-dimensional wind field from multiple-Doppler bistatic radar network data. *J. Atmos. Oceanic Technol.*, **16**, 432–449, https://doi.org/10.1175/1520-0426(1999)016<0432:AVMFRT>2.0.CO;2.

——, and J. S. Soderholm, 2020: 27/11/2014 Brisbane HailTrack case study data. Australian Bureau of Meteorology, accessed 1 November 2020, https://doi.org/10.5281/zenodo.3600107.

Rasmussen, R. M., and A. Heymsfield, 1987: Melting and shedding of graupel and hail. Part II: Sensitivity study. *J. Atmos. Sci.*, **44**, 2764–2782, https://doi.org/10.1175/1520-0469(1987)044<2764:MASOGA>2.0.CO;2.

——, V. Levizzani, and H. R. Pruppacher, 1984: A wind tunnel and theoretical study on the melting behavior of atmospheric ice particles: III. Experiment and theory for spherical ice particles of radius > 500 μm. *J. Atmos. Sci.*, **41**, 381–388, https://doi.org/10.1175/1520-0469(1984)041<0381:AWTATS>2.0.CO;2.

Richter, H., and R. Deslendes, 2007: The four large hail assessment techniques in severe thunderstorm warning operations in Australia. *33rd Conf. on Radar Meteorology*, Cairns, QLD, Australia, Amer. Meteor. Soc., P5.19, https://ams.confex.com/ams/pdfpapers/123766.pdf.

——, J. Peter, and S. Collis, 2014: Analysis of a destructive wind storm on 16 November 2008 in Brisbane, Australia. *Mon. Wea. Rev.*, **142**, 3038–3060, https://doi.org/10.1175/MWR-D-13-00405.1.

Ryzhkov, A. V., and D. S. Zrnić, 2019: *Radar Polarimetry for Weather Observations*. Springer, 486 pp.

——, T. J. Schuur, D. W. Burgess, and D. S. Zrnić, 2005: Polarimetric tornado detection. *J. Appl. Meteor.*, **44**, 557–570, https://doi.org/10.1175/JAM2235.1.

——, M. R. Kumjian, S. M. Ganson, and A. P. Khain, 2013a: Polarimetric radar characteristics of melting hail. Part I: Theoretical simulations using spectral microphysical modeling. *J. Appl. Meteor. Climatol.*, **52**, 2849–2870, https://doi.org/10.1175/JAMC-D-13-073.1.

——, ——, ——, and P. Zhang, 2013b: Polarimetric radar characteristics of melting hail. Part II: Practical implications. *J. Appl. Meteor. Climatol.*, **52**, 2871–2886, https://doi.org/10.1175/JAMC-D-13-074.1.

Sander, J., J. F. Eichner, E. Faust, and M. Steuer, 2013: Rising variability in thunderstorm-related U.S. losses as a reflection of changes in large-scale thunderstorm forcing. *Wea. Climate Soc.*, **5**, 317–331, https://doi.org/10.1175/WCAS-D-12-00023.1.

Schaefer, J. T., 1990: The critical success index as an indicator of warning skill. *Wea. Forecasting*, **5**, 570–575, https://doi.org/10.1175/1520-0434(1990)005<0570:TCSIAA>2.0.CO;2.

Schiesser, H. H., 1990: Hailfall: The relationship between radar measurements and crop damage. *Atmos. Res.*, **25**, 559–582, https://doi.org/10.1016/0169-8095(90)90038-E.

Schmid, W., H. H. Schiesser, and A. Waldvogel, 1992: The kinetic energy of hailfalls. Part IV: Patterns of hailpad and radar data. *J. Appl. Meteor.*, **31**, 1165–1178, https://doi.org/10.1175/1520-0450(1992)031<1165:TKEOHP>2.0.CO;2.

Schuster, S. S., R. J. Blong, and K. J. McAneney, 2006: Relationship between radar-derived hail kinetic energy and damage to insured buildings for severe hailstorms in eastern Australia. *Atmos. Res.*, **81**, 215–235, https://doi.org/10.1016/j.atmosres.2005.12.003.

Smith, P. L., and A. Waldvogel, 1989: On determinations of maximum hailstone sizes from hailpad observations. *J. Appl.*

Meteor., **28**, 71–76, https://doi.org/10.1175/1520-0450(1989)028<0071:ODOMHS>2.0.CO;2.

Snook, N., Y. Jung, J. Brotzge, B. Putnam, and M. Xue, 2016: Prediction and ensemble forecast verification of hail in the supercell storms of 20 May 2013. *Wea. Forecasting*, **31**, 811–825, https://doi.org/10.1175/WAF-D-15-0152.1.

Soderholm, J. S., H. A. McGowan, H. Richter, K. Walsh, T. Wedd, and T. M. Weckwerth, 2017: Diurnal preconditioning of subtropical coastal convective storm environments. *Mon. Wea. Rev.*, **145**, 3839–3859, https://doi.org/10.1175/MWR-D-16-0330.1.

Warren, R. A., H. A. Ramsay, S. T. Siems, M. J. Manton, J. R. Peter, A. Protat, and A. Pillalamarri, 2019: Radar-based climatology of damaging hailstorms in Brisbane and Sydney, Australia. *Quart. J. Roy. Meteor. Soc.*, **146**, 505–530, https://doi.org/10.1002/QJ.3693.

Wilson, C., K. Ortega, and V. Lakshmanan, 2009: Evaluating multi-radar, multisensor hail diagnosis with high resolution hail reports. *25th Conf. on Interactive Information Processing Systems*, Phoenix, AZ, Amer. Meteor. Soc., P2.9, https://ams.confex.com/ams/pdfpapers/146206.pdf.

Witt, A., M. D. Eilts, G. J. Stumpf, J. T. Johnson, E. D. W. Mitchell, and K. W. Thomas, 1998: An enhanced hail detection algorithm for the WSR-88D. *Wea. Forecasting*, **13**, 286–303, https://doi.org/10.1175/1520-0434(1998)013<0286:AEHDAF>2.0.CO;2.

Zhang, C., Q. Zhang, and Y. Wang, 2008: Climatology of hail in China: 1961–2005. *J. Appl. Meteor. Climatol.*, **47**, 795–804, https://doi.org/10.1175/2007JAMC1603.1.

Ziegler, C. L., P. S. Ray, and N. C. Knight, 1983: Hail growth in an Oklahoma multicell storm. *J. Atmos. Sci.*, **40**, 1768–1791, https://doi.org/10.1175/1520-0469(1983)040<1768:HGIAOM>2.0.CO;2.